Chinese Journal of Mechanical Engineering

**ORIGINAL ARTICLE**                                                    **Open Access**

# Numerical Simulation and Experimental Verification of Laser Multi-Section Welding

Jia Liu[1,2,3*] , Tao Jiang[1,2,3], Yan Shi[1,2,3], Hongyin Zhu[1,2,3] and Yuchi Dai[1,2,3]

## Abstract

To address the problems of large welding deformation and splashing in the resistance spot welding of the lubricating oil cooler plate, the laser spot welding was employed, instead of the resistance spot welding, and a novel laser spot welding was proposed, i.e., laser multi-section welding. The major processes involved in this study referred to a finite element model of pulsed laser lap welding built by adopting SYSWELD simulation software, as well as the laser welding of various welding methods. The effect of different welding methods on the welding quality was studied, the parameters of the average power and the duty cycle were optimized in line with the comparative analysis of the experimentally achieved results and the numerical simulation. As indicated from the experimentally achieved results, when the new 6-sections welding method was adopted, the resulting welded joint achieved the most uniform heat input and the largest welding fusion area, and the tensile properties exhibited by the welded joints were significantly enhanced, whereas some pores remained. By altering the duty cycle, pores could be eliminated to further improve the quality of the joint. The mentioned process method could tackle down the problems facing conventional resistance spot welding. Furthermore, it was capable of improving the uneven heat input of the laser spot welding.

**Keywords:** Laser multi-section welding, SYSWELD, Finite element analysis, Mechanical properties

## 1 Introduction

A lubricating oil cooler refers to an extensively applied heat exchanger that critically impacts nuclear power, chemical industry and other relevant fields, which can reduce energy loss to a certain extent [1]. Figure 1 presents a structural diagram of a lubricating oil cooler. Austenitic stainless steel has been broadly applied in railway vehicles and the heat exchanger/chemical industry for their prominent corrosion resistance, high strength and efficient stamping performance [2–5]. Currently, the lube oil cooler plate primarily employs the resistance spot welding for connection, whereas serious spatter issues exist in such a welding process, As shown in Figure 2. Besides, the resistance spot welding exhibits the defects below. First, when welding one of the points,

a part of the current tends to flow through the welded solder joints, which reduces the quality of the welding. Next, the resistance of the electrode and the workpiece are easy to be affected by considerable factors (e.g. such as temperature, electrode pressure and other material properties), thereby causing the resistance spot welding to be extremely vulnerable to outside conditions, Moreover, the requirements of cleanliness are high. In the presence of impurities on the surface, the resistance between the weldments will increase significantly, thereby directly affecting its conductivity features. For the mentioned reasons, the laser welding technology is proposed to replace the original resistance spot welding.

Laser welding is recognized as an efficient and precise welding method that exploits a high energy density laser beam as the heat source. It is advantageous for its high energy density, as well as for its precise focus, strong penetrating ability, high welding efficiency and applicability since applies to a myriad of materials. Currently, it is mostly employed in aerospace, automotive,

*Correspondence: liujia@cust.edu.cn

[1] School of Electromechanical Engineering, Changchun University of Science and Technology, Changchun 130022, China
Full list of author information is available at the end of the article

Liu *et al. Chinese Journal of Mechanical Engineering*　　(2022) 35:125

Page 2 of 15



**Figure 1** Lubricating-oil cooler
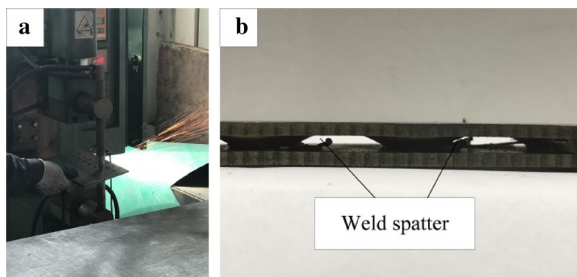


**Figure 2** Resistance spot welding process and internal section photos of the sealed cavity: **a** Spatter during welding; **b** Deposition of splashes in the cavity

microelectronics and nuclear industries with high precision and high-quality welding areas [6–9]. Compared with resistance spot welding, laser spot welding has many advantages, such as high welding accuracy, accurate energy control, and good penetration. With the use of the non-contact welding, the welding quality can be ensured for the welding of complex structures, and the application turns out to be more flexible. However, the laser spot welding, as a cutting-edge spot welding method, still faces many unsolved technical problems. The laser spot welding will cause stress concentration and uneven heat inputs. Moreover, as impacted by the extremely fast heating and cooling speeds, extreme defects (e.g., pores and cracks) are easy to produce, which seriously reduces the quality of the weld formation and the weld strength [10–13].

Finite element simulation can be adopted at the initial stage of design since it acts as a powerful tool for experiment and optimization in virtual environments. Besides, such a technique can help reduce the number of experiments and lay a theoretical basis for strength analyses [14–17].

Yan et al. [18] studied the structure and mechanical properties of 304 stainless steel joints welded by tungsten inert gas (TIG) welding, laser welding, and laser-TIG hybrid welding. The results of his experimentations show that the laser-welded joint has the highest tensile strength and the smallest dendrite size among all, while the TIG welded joint has the lowest tensile strength and the largest dendrite size. Chakravarthy et al. [19] also studied the effect of laser welding process parameters and welding speed on the welding performance of 70/30 Cu-Ni alloy welded joints. His processes proved that, when the laser uses a welding speed of 1.5 m/min, the joints produced fine, equiaxed, and uniformly distributed grains that have better mechanical properties than other joints in the fusion zone. Going further, Bowen Liu et al. [20] studied the dual laser beam welding of 316L austenitic stainless steel, using an artificial neural network (ANN) and genetic algorithm (GA) to obtain the best welding parameters of them. Some other studies have shown that porosity features are significantly reduced compared to the original weld. Derakhshan et al. [21] examined the effects of heat input on mechanical properties obtained by four different welding processes: Autogenous Laser Welding, Cold Wire Assisted Laser Welding, Hybrid Laser Arc Welding, and traditional Submerged Arc Welding. SYSWELD software was used to predict the temperature field, residual stress, and deformation and the experimental results had a satisfactory correlation with the calculated results. The process proved that, by increasing the cooling rate of the welding process, it is possible to effectively improve the microhardness of the weld center. Adding to that, Saravanan et al. [22] compared the macrostructures of Hastelloy C-276 joints obtained by Nd: YAG laser butt-welding through numerical simulation and experimental methods. The results show that SYSWELD is suitable for simulating the weld profile and temperature distribution of laser-welded Hastelloy C-276 joints. In this case, the profile obtained by the numerical simulation was also very consistent with the experimental results. Last but not least, Ganesh et al. [23] performed the thermo-mechanic analysis using SYSWELD and both residual stress and distortion predicted by FEM simulation were in acceptable agreement with the experimental measurements.
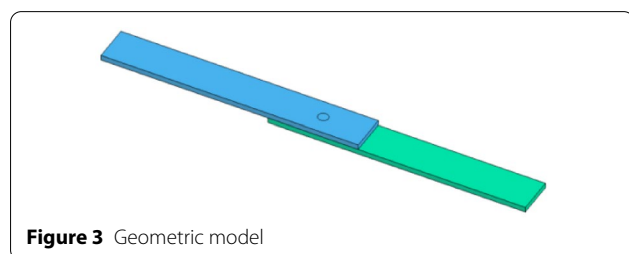
Since the lubricating oil cooler has higher requirements for heat exchange efficiency, it is desirable to have the greatest strength under the identical welding area to avoid the excessive welding area from affecting the flow of the fluid media and affecting the heat transfer. On that basis, this study proposed a novel laser welding method (multi-section welding) for the plate heat exchanger welding. Such a welding method was used instead of the laser spot welding. The welding path was segmented,

Liu *et al. Chinese Journal of Mechanical Engineering*    (2022) 35:125

Page 3 of 15

and its laser parameters were optimized, which avoided the spatter produced by the conventional spot welding. Moreover, the welding heat input turned out to be uniform and satisfied the requirements of use. This study primarily employed a combination of numerical simulation and experiments to study the effect of different welding methods on the weld pool morphology, the fracture morphology and the mechanical properties of the joint. Next, the parameters were further optimized. Hopefully, the study of such a laser welding method can provide researchers and industrial engineers with more insights.

## 2  Materials and Methods

First, 304 austenitic stainless steel plates with the dimension of 100 mm×15 mm×2 mm acted as the welding base metal. The length of the lap joint area was 35 mm, and the diameter of the circular weld was 4 mm, as shown in Figure 3. The detailed composition of base metal is listed in Table 1. Before the welding, the impurities on the surface of the workpiece should be cleaned with acetone reagent.

The laser welding system was composed of TruDisk 8002 laser and KUKA robot. After the welding, the sample was cut to perform a tensile test. Besides, there are three samples for the respective experimental parameter. The average value was taken to determine the final average tensile shear force. Furthermore, a stereomicroscope was employed to photograph the fracture morphology of the stretched sample and to observe the morphology and fusion state of the combined surface of the welded joint. Moreover, a metallographic sample was prepared, and a metallographic microscope was employed to characterize the weld morphology under a metallographic microscope, as well as to measure the depth and width of fusion simultaneously. The observation method is illustrated in Figure 4. Such an observation direction was applied when different laser welding methods were employed.

To ensure the weld strength, the overall penetration depth of the laser welding was controlled in the range of 3±0.2 mm. The different power parameters for segmental welding are listed in Table 2. The welding sequence from the center of the circle to the end of it and four welding methods (i.e., 1-section, 4-sections, 5-sections, and 6-sections) were adopted. The detailed schematic diagram of welding is shown in Figure 5.

## 3  Finite Element Analysis

### 3.1  Establishment of Heat Source Modes

Notably, the heat source should be checked prior to the simulation calculation to make the result more accurate. The 3D Gaussian heat source was selected regardless of the flow of the molten pool, and the energy distribution of the temperature field of the source is presented in Figure 6. According to the figure, the heat flow energy in the middle was high, and the surroundings were low, so the heat source might display a Gaussian distribution.

In Figure 6, $Q_0$ denotes the maximum input energy density; $r_e$ and $r_i$ are Gaussian parameters, where $r_e$ represents the maximum characteristic radius on the plane $z=z_e$, and $r_i$ denotes the maximum characteristic radius on the plane $z=z_i$; $z_e$ and $z_i$ express are the



**Figure 3** Geometric model
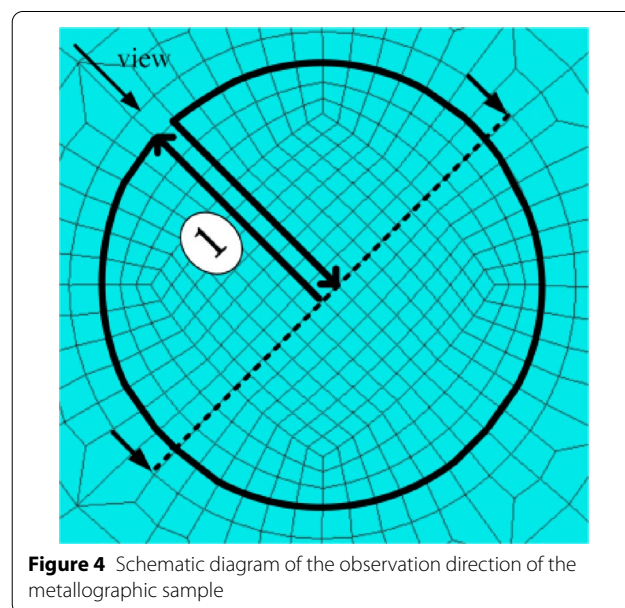


**Figure 4** Schematic diagram of the observation direction of the metallographic sample

**Table 1** Chemical composition of 304 stainless steel (mass ratio, %)

| C | Si | Mn | P | Ni | Cr | N | Fe |
|---|---|---|---|---|---|---|---|
| ≤ 0.08 | ≤ 0.75 | ≤ 2.0 | ≤ 0.045 | 8.0–10.5 | 18.0–20.0 | ≤ 0.1 | Bal. |

Liu *et al. Chinese Journal of Mechanical Engineering*        (2022) 35:125

Page 4 of 15

**Table 2** Process parameters of different welding methods

| Welding type | Average power (W) | Defocus (mm) | Duty cycle (%) | Welding speed (m/min) | Impulse frequency (Hz) | Shielding gas flow (L/min) |
|---|---|---|---|---|---|---|
| 1-section | 2100 | + 4 | 50 | 1.5 | 40 | 25 |
| 4-sections | 2500/2400/1700/800 | + 4 | 50 | 1.5 | 40 | 25 |
| 5-sections | 2500/2375/2200/1650/750 | + 4 | 50 | 1.5 | 40 | 25 |
| 6-sections | 2500/2350/2350/1975/1600/725 | + 4 | 50 | 1.5 | 40 | 25 |
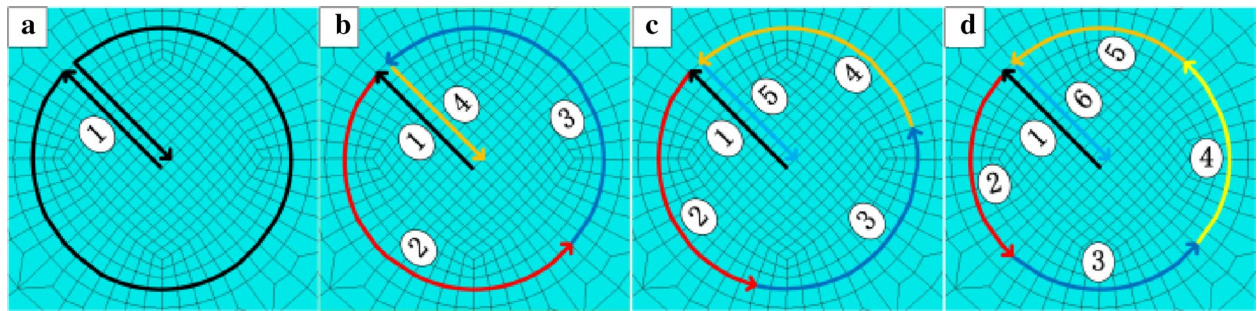


**Figure 5** Schematic diagram of laser overlap welding method: **a** 1-section; **b** 2-sections; **c** 3-sections; **d** 4-sections
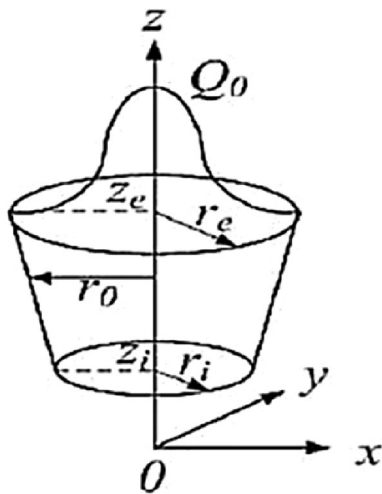


**Figure 6** 3D Gaussian heat source

3D Gaussian heat sources. The position makes a parameter with the surface of the piece to be welded, where $z_i$ denotes the relative height difference between the upper surface of the 3D Gauss heat source and the surface of the workpiece, and $z_i$ is the relative height difference between the lower surface of the 3D Gauss and the surface, positive above the outward. This is also likely to be negative. Thus, the parameter relation can be expressed as [24–27]:

$$r_0(z) = r_e - (r_e - r_i)\frac{z_e - z}{z_e - z_i}. \tag{1}$$

For the numerical simulation of the laser welding, the total energy of the 3D Gaussian heat source is written as:

$$Q = \eta P. \tag{2}$$

Therefore, when using a 3D Gaussian heat source to simulate laser welding, the energy distribution is represented as:

$$q(r,z) = \frac{9\eta P e^3}{\pi H(e^3 - 1)(r_e^2 + r_e r_i + r_i^2)}\exp\left(-\frac{3r^2}{r_0^2}\right). \tag{3}$$

In Eq. (1), $r_0(z)$ is the maximum radius of action on the plane of height $z$. Eq. (2) can be used to calculate the total energy of the heat source when using a 3D Gaussian heat source to simulate laser welding. In this case, $Q$ is the total energy of the heat source; $\eta$ is the absorption rate of the metal to the laser and $P$ stands for the laser power. Last, Eq. (3) addresses the energy distribution of 3D Gaussian heat source simulating laser welding where $q(r,z)$ represents the energy density from the center $r$ on the plane of height $z$ and $H$ is the total height of the heat source.

In SYSWELD, the heat source parameters can be calculated from the actual weld profile. Here, the welded joint profile parameters of the single-pass weld optimized by previous experiments are used as the basis for calculating

Liu *et al. Chinese Journal of Mechanical Engineering*        (2022) 35:125

Page 5 of 15
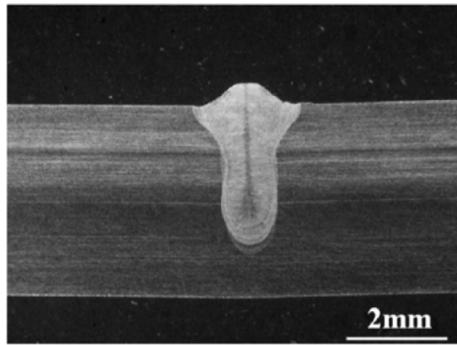


**Figure 7** Shape of the welded joint of single-pass weld

the heat source parameters, which can effectively reduce the optimization of the heat source parameters. The morphology of the single-pass weld pool was obtained with a laser power of 2500 W, a pulse frequency of 40 Hz, and a welding speed of 1.5 m/min is shown in Figure 7. The weld width is 2.35 mm, the penetration depth is 2.94 mm, and the joint surface width is 1.2 mm. Input data to SYSWELD Among them, the heat source parameters obtained by the feedback were $r_e = 1.175$, $r_i = 0.6$, $z_e = 0$, $z_i = -2.94$. This heat source parameter was applied to

laser multi-section welding. Using the 1-section welding method, the laser parameters included the laser power of 1800 W, the defocus of $+ 4$ mm, the welding speed of 1.5 m/min. According to Figure 8, as indicated from the comparison, the morphology of the molten pool in the numerical simulation was identical to that of the actual welded joint, the accuracy of the selected heat source model and heat source parameters could be verified.

### 3.2 Establishment of the Finite Element Model

The energy density generated by the laser welding is extremely high, and the heating speed is fast. When the weld is locally heated, the temperature difference between the weld and the surrounding area turns out to be significantly large. However, in the area far away from the weld, the temperature distribution is basically insignificant. Based on the characteristics of the temperature distribution of the laser welding, when meshing, a finer mesh is required in the weld area and its vicinity. The meshing result of the welded specimen is presented in Figure 9. To improve the calculation accuracy, the grid division should be relatively fine in and fit around the weld zone. Here, the minimum grid size was 0.2 mm during the grid division, so the result of the temperature field was more accurate. In the area far from the weld,
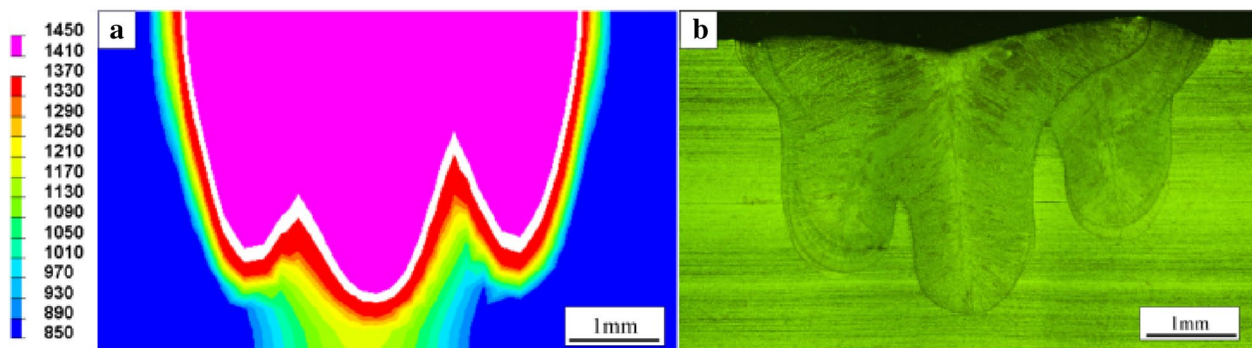


**Figure 8** Comparison of weld morphology of welded joints: **a** Numerical simulation of the molten pool morphology; **b** Actual weld joint morphology
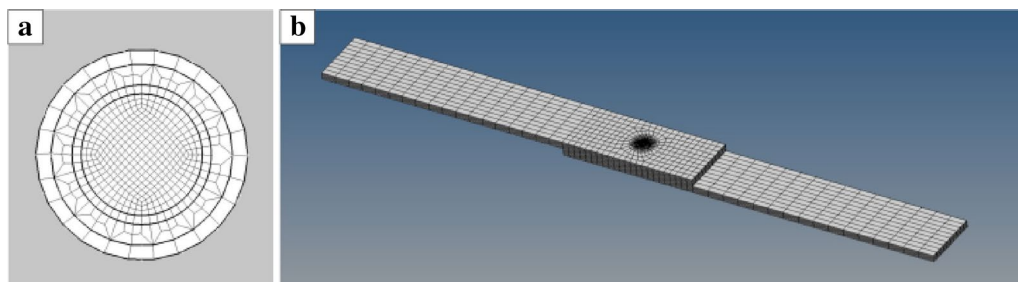


**Figure 9** Meshing result of the welded specimen: **a** Grid within the weld; **b** Overall grid

Liu *et al. Chinese Journal of Mechanical Engineering*      (2022) 35:125

Page 6 of 15

the maximum mesh size reached 4 mm, thereby leading to a reduced number of grids and calculation time, while the small and big mesh were connected via the transition mesh.

## 4 Results and Discussion

### 4.1 Numerical Simulation and Experimental Comparison

The welding experiments were performed according to the welding parameters (Table 2). In addition, the simulated molten pool morphology should be compared with the actual joint morphology when the welding experiment was completed. The diameter of the circular weld was 4 mm, so a cylinder with a diameter of 4 mm was taken for the temperature field observation, and the change depth of fusion could be observed directly. The temperature field cloud diagram obtained when the welding method was 1-section is presented in Figure 10. According to the figure, the depth of fusion tended to increase, with a change range of 3–3.38 mm. The alterations were attributed to the different temperatures on the workpiece, as impacted by the action of the moving heat source during the welding. The moving heat source

exhibited a significant performance on each position of the welding due to the circular welding path and the small diameter of the circumference. Accordingly, the secondary heating exerted a superimposed effect on the weld, thereby resulting in a greater change in the depth of fusion.

The joint morphology with the welding mode of 1-section shown in Figure 11 helped to closely observe the differences in the depth of fusion. In the figure, the molten pool morphology of numerical simulation was identical to the morphology of the actual welded joint, but the range of weld penetration is way too large to meet the experimental requirements. Besides, no further discussion would be conducted.

Considering the 4, 5, and 6-sections of welding, the temperature field distribution cloud diagrams obtained are shown in Figures 12, 13 and 14, respectively. As observed from the figures, the welding process was the most stable one and the variation range (3–3.12 mm) of the depth of fusion was the smallest when the 6-section welding method was adopted. In addition, the morphology of the welded joint is presented in Figures 15, 16 and
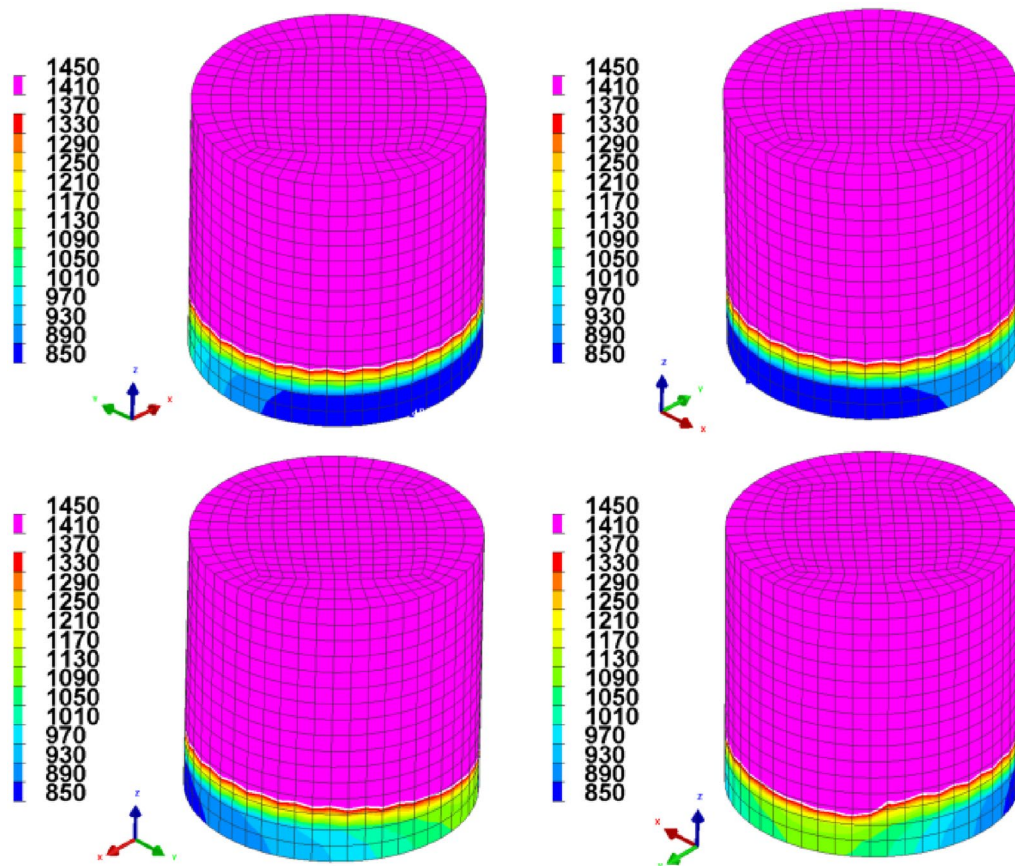


**Figure 10** Temperature field distribution cloud map under the welding condition of 1-section

Liu *et al. Chinese Journal of Mechanical Engineering* (2022) 35:125

Page 7 of 15
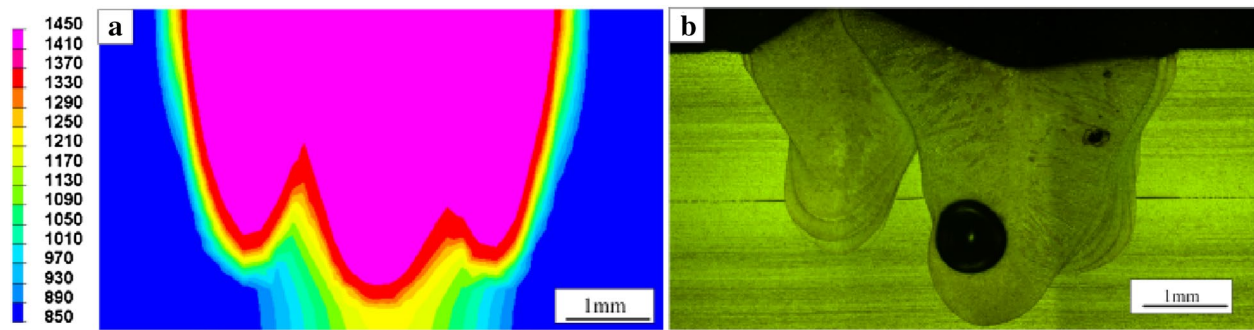


**Figure 11** Welding method is a 1-section of joint morphology: **a** Numerical simulation of molten pool morphology; **b** Actual welded joint morphology
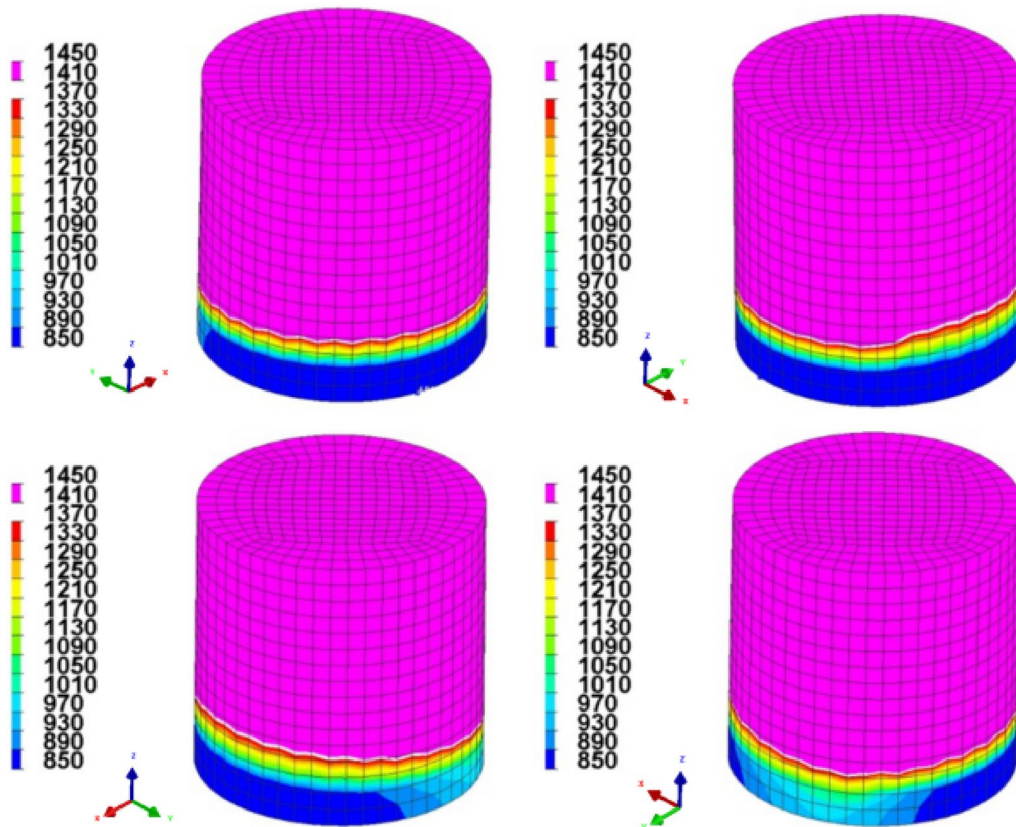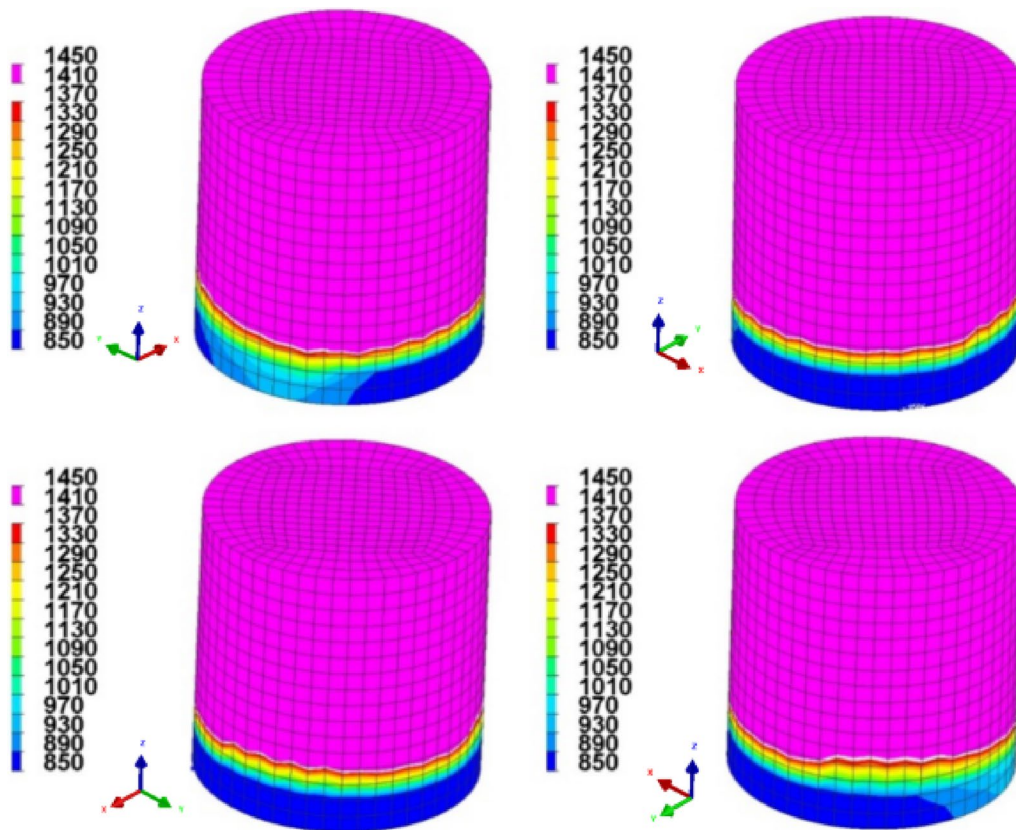


**Figure 12** Temperature field distribution cloud map under the welding condition of 4-sections

17, thereby proving that the depth of fusion was maintained at about 3 mm. The optimal welding effect was achieved when the 6-sections welding method was adopted.

Figure 18 illustrates the temperature field of the welded combined surface and in the area enclosed by the welding path, the overall fusion was better. However, there is still a small part of the unfused areas. It was also

observed that the incomplete fused positions at the combined surface of the welding joint were all around the welding starting point. The welding method of the 6-sections changed to a new welding path as shown in Figure 19, that is, the length of the initial welding section is increased from 2 mm to 3 mm (new 6-sections), while the other paths remained the same. The corresponding average power of each section also changed—to

**Figure 13** Temperature field distribution cloud map under the welding condition of 5-sections

2500/2350/2150/1975/1600/725 W—while other process parameters had no alterations. The final welding joint morphology obtained is shown in Figure 20, and it was achieved after a numerical simulation calculation of the temperature field and laser welding experiment. In this stage, the morphological properties are consistent with those of the actual welding joint, and the depth of fusion of the molten pool is about 3 mm. Figure 21 is the combined surface temperature field of the welded joint obtained by the new 6-sections welding method, the welded combined surface was completely fused. which might meet all the experimental requirements.

## 4.2 Mechanical Properties

To study the effect of different welding methods on the mechanical properties of weld joints, tensile experiments were performed on welded joints obtained under sections 4, 5, 6, and new 6-sections. According to Figure 22, the tensile shear force obtained by the 6-section welding method was significantly improved compared with the 4-sections and 5-sections welding methods, which reached over 10256 N. Under the new 6-sections

welding method, the tensile shear force performance of the welded joint was further improved, the average tensile shear force of the welded joint was 10454 N, and the maximum tensile force increased by 2% compared with the one obtained by 6-section welding. It was therefore indicated that the mechanical properties of this process were up to the mark.

To explore the reasons for the different tensile properties caused by using different welding methods, it was necessary to conduct a numerical simulation analysis and an experimental verification of the temperature field at the joint surfaces should be performed. The way of tensile fracture is shown in Figure 23, fracture positions were all at the combined surface. Figure 24 shows the tensile fracture morphology of the welded joint, and the existence of the area without fusion on the combined surface of the weld was consistent with the results of the temperature field simulation in Figures 18 and 21. Also, the area of the fusion zone obtained in the 4, 5, 6, and new 6-sections methods were 15.95 mm$^2$, 15.88 mm$^2$, 17.50 mm$^2$, and 17.97 mm$^2$, respectively, as shown in Figure 25. Thus, it can be concluded that the fusion area of combined surface and mechanical
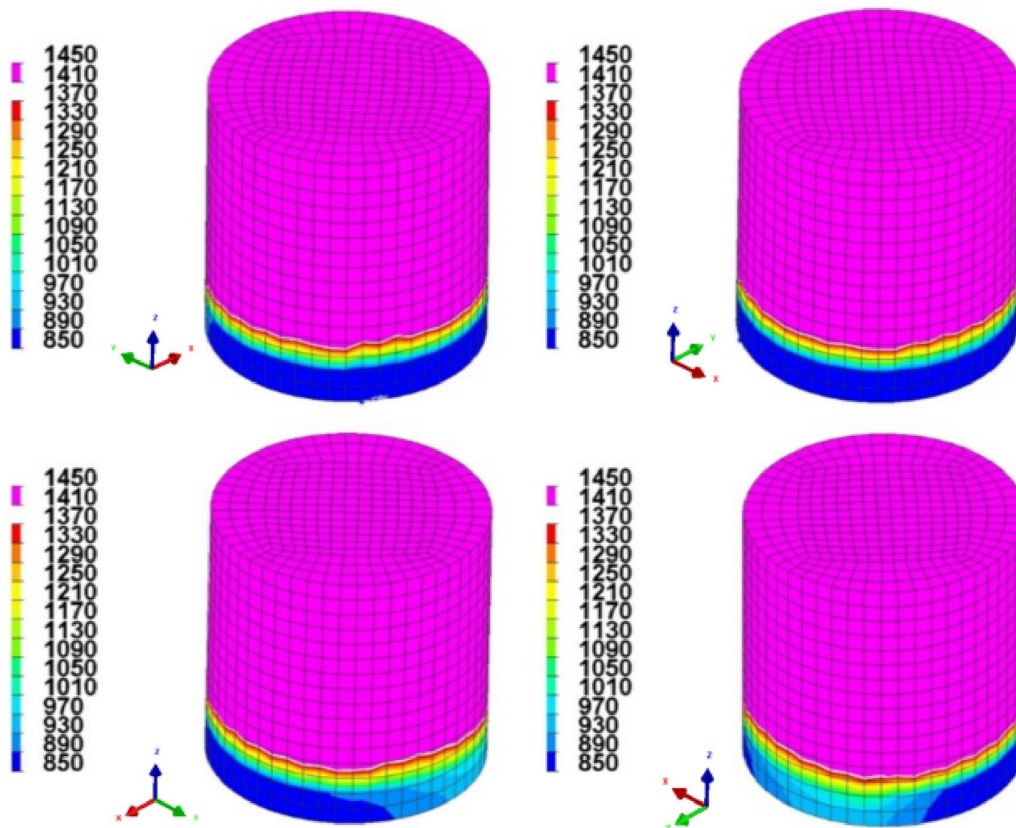
**Figure 14** Temperature field distribution cloud map under the welding condition of 6-sections
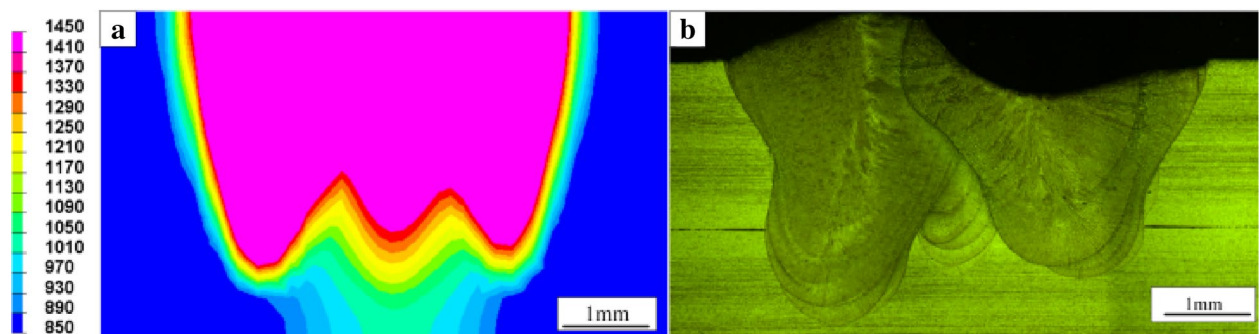


**Figure 15** Welding method is 4-sections of joint morphology: **a** Numerical simulation of molten pool morphology; **b** Actual welded joint morphology

properties of welded joints was greatly improved under the welding method based on the new 6-sections welding.

### 4.3 Process Parameter Optimization

After the observation and analysis of the welded joint obtained by using the new 6-sections welding method,

a small number of pores could still be identified. In the pulse laser welding, laser transmission behavior showed significant differences with the variation of the duty cycle, which significantly affected the weld appearance and formation of stomata [28–30]. The porosity was reduced by changing the duty cycle, thereby further

Liu *et al. Chinese Journal of Mechanical Engineering*        (2022) 35:125

Page 10 of 15
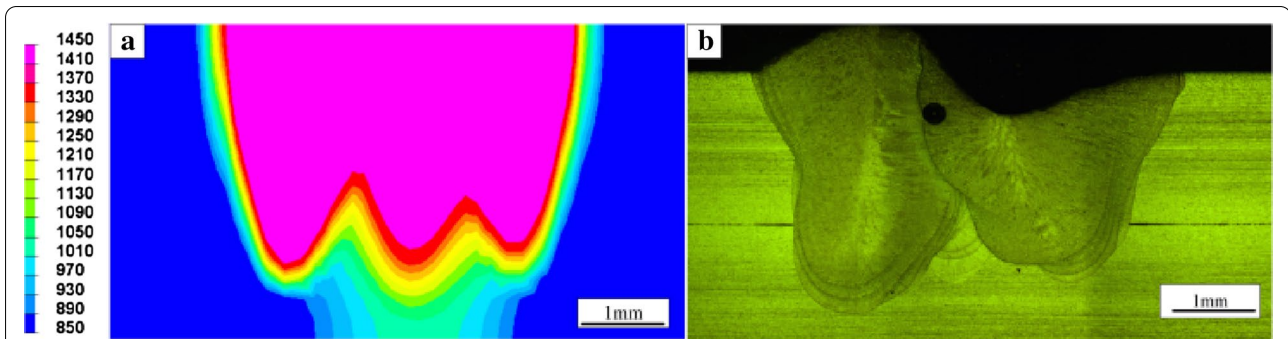


**Figure 16** Welding method is 5-sections of joint morphology: **a** Numerical simulation of molten pool morphology; **b** Actual welded joint morphology
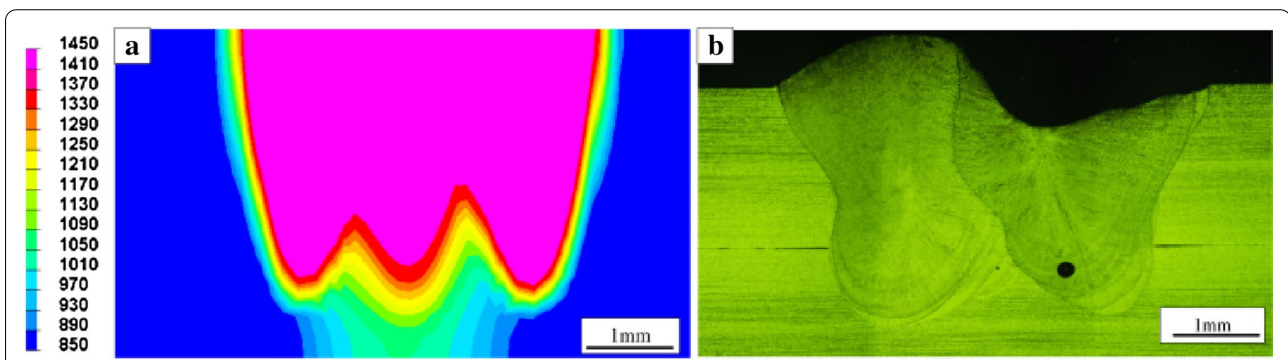


**Figure 17** Welding method is 6-sections of joint morphology: **a** Numerical simulation of molten pool morphology; **b** Actual welded joint morphology
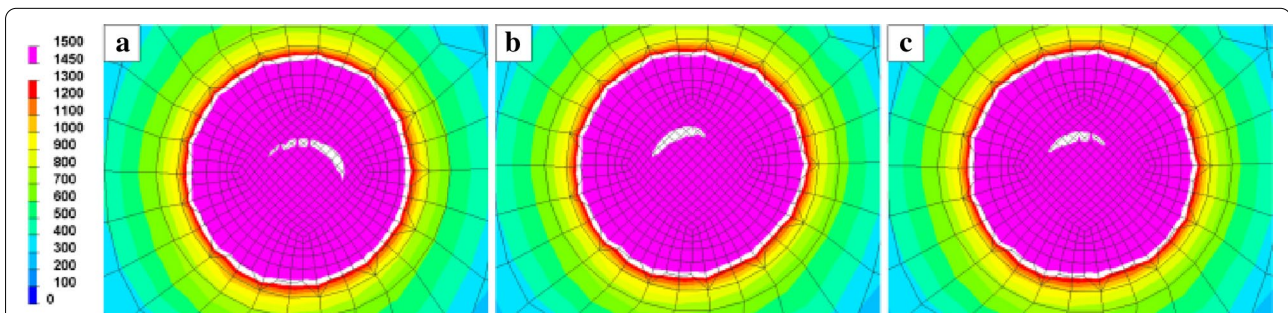


**Figure 18** Temperature field of combined surface under different welding methods: **a** 4-sections; **b** 5-sections; **c** 6-sections

improving the quality of the welded joint. The specific welding process parameters are listed in Table 3.

Figure 26 presents the weld morphology of welded joints under different duty cycles. Figures 27 and 28, respectively represent the fusion area and tensile shear force of the welded joint also in different duty cycles. According to the figures, when the duty cycle is increased from 35% to 46%, the fusion area of the welded joint remained basically the same—maintained at about 18.5

$mm^2$. However, when the duty cycle was 35%, the tensile shear of the welded joint was significantly reduced. When the duty cycle was small, a high-power density laser beam acted on the workpiece to instantly vaporize the metal to form a keyhole, while considerable plasma was generated to shield the absorption of laser energy by the molten pool with the increase in the duty cycle. Though the power density of the laser was weakened, the plasma generated was also reduced, whereas the absorption rate
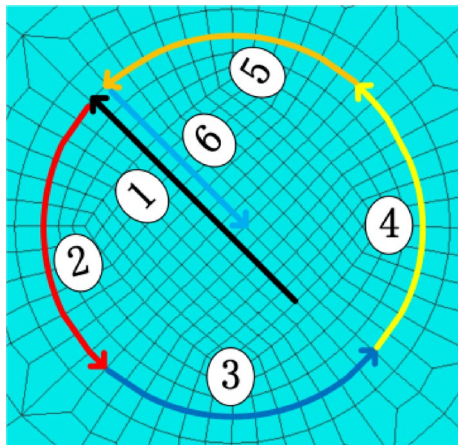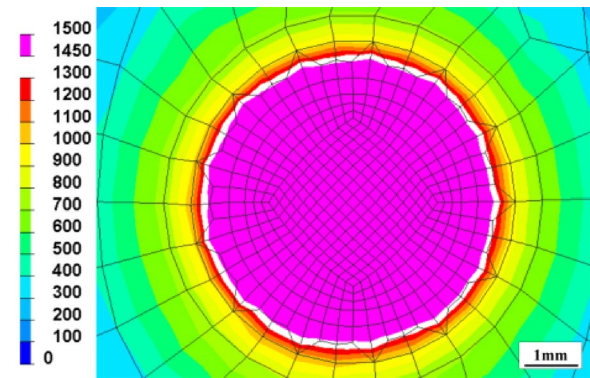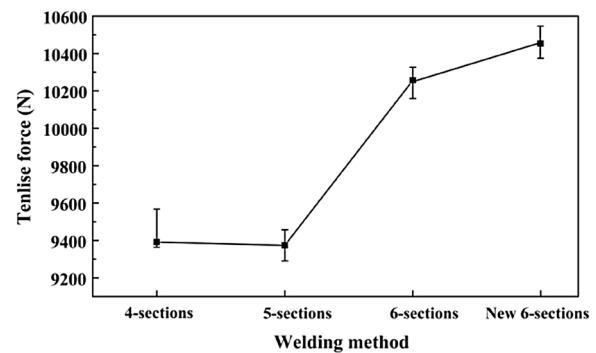
**Figure 19** Welding method is the new 6-sections welding path



**Figure 21** Welding method is the combined surface temperature field of the new 6-sections welding joint

of the laser energy by the molten pool increased. Lastly, the heat obtained at the combined surface was not so divergent, thereby causing the insignificant change of the fusion area at the combined surface. When the duty cycle was 35%, the power density of the laser spot was extremely high, and a large amount of metal vapor was generated. Due to the small pulse width, the laser acted on the workpiece only for a short time, and the weld pool rapidly cooled and solidified. At this stage, it was too late for the metal vapor to escape, making it easier to form porosity defects. Combined with the tensile fracture morphology of the welded joint shown in Figure 29, it can be said that there were larger porosity defects at the tensile fracture with a duty cycle of 35%, therefore, the tensile properties of the welded joint were reduced.

During the duty cycle from 46% to 75%, as it increased, the tensile shear force of the welded joint was gradually reduced. An increased duty cycle caused the laser power density to continue to downgrade, thereby resulting in a reduction in the fusion area of the combined surface. When the duty cycle was between 54% and



**Figure 22** The maximum tensile force of welded joints under different welding methods

58%, the fusion area was nearly equal, whereas the tensile shear force of the welded joint differed by about 220 N. This was because in this scenario, the power density of the pulsed laser was lower, so the generated energy was insufficient to maintain the stable existence of the keyhole. Consequently, the keyhole collapse was easy to
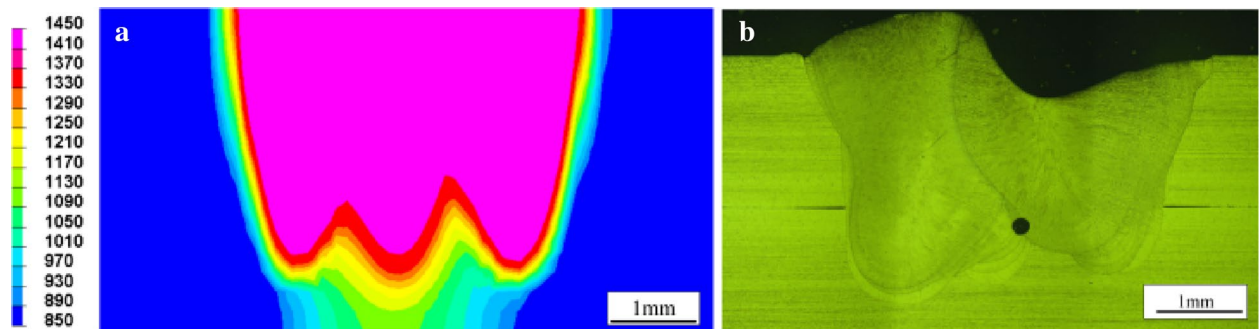


**Figure 20** Weld joint morphology of new 6-sections: **a** Numerical simulation of molten pool morphology; **b** Actual welded joint morphology
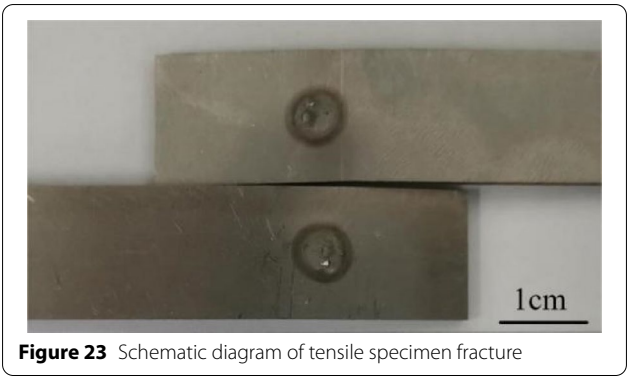
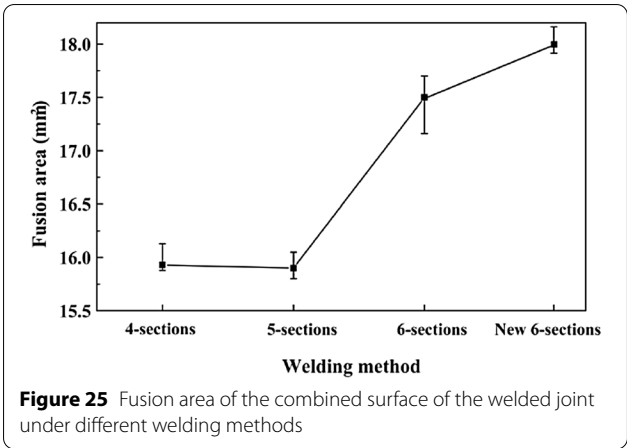**Figure 23** Schematic diagram of tensile specimen fracture



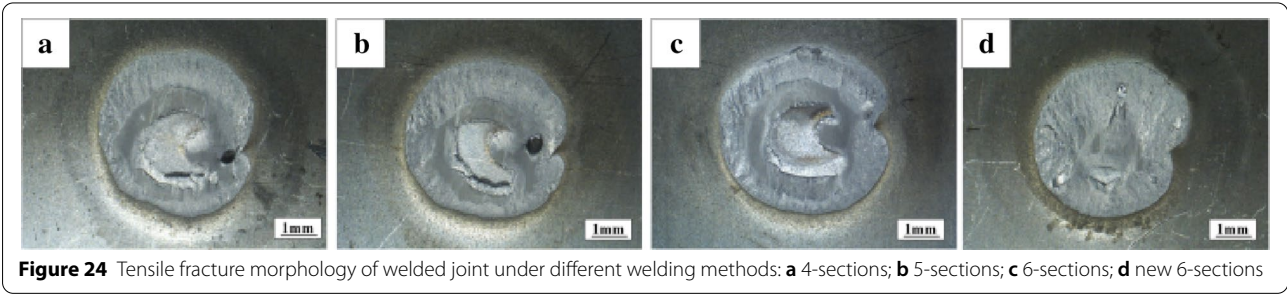**Figure 25** Fusion area of the combined surface of the welded joint under different welding methods



**Figure 24** Tensile fracture morphology of welded joint under different welding methods: **a** 4-sections; **b** 5-sections; **c** 6-sections; **d** new 6-sections

occur, thereby causing the gas to stay in the weld, which led to the formation of the pore defect. This phenomenon happens precisely due to the pores at the tensile fracture that the welded joint was pulled, causing the reduction of tensile shear force. When the duty cycle is increased to 75%, the laser power density is extremely low. It can be seen from the topography that there are large unfused areas and multiple pore defects at the joint surface, thereby weakening the tensile properties of welded joints. Based on the above analysis it is possible to state that, when the selected duty cycle is 42% to 46%, the best quality welded joint is obtained with a maximum tensile shear force of about 10632 N. As shown in Figure 30, the new

6-sections welding method and the 45% duty cycle were adopted to conduct the welding experiments on the trial plate pairs of the lubricating oil cooler. The welding seam quality was good, and there was no splash in the welding cavity, which fully met the experiment.
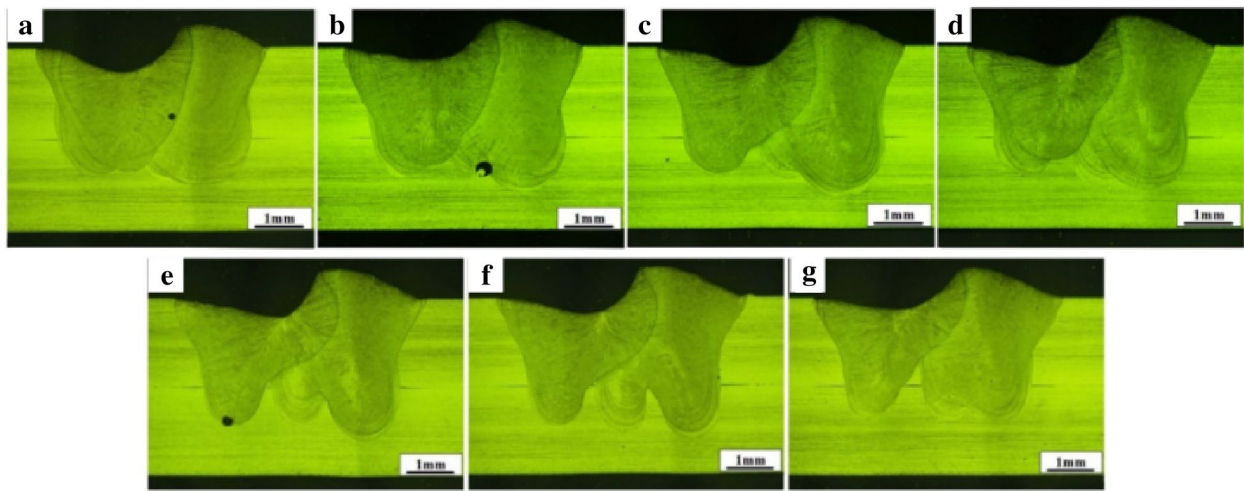
## 5 Conclusions

Given the major results of the experiments conducted here, some main conclusions could be drawn after all the processes were achieved:

(1) By comparing the simulation results of different welding methods, it was concluded that the opti-

**Table 3** Process parameters under different duty cycles

| Welding type | Duty cycle (%) | Average power (W) | Welding speed (m/min) | Impulse frequency (Hz) | Defocus (mm) | Shielding gas flow (L/min) |
|---|---|---|---|---|---|---|
| New 6-sections | 35 | 2500/2350/2150/1975/1600/725 | 1.5 | 40 | + 4 | 25 |
| New 6-sections | 42 | 2500/2350/2150/1975/1600/725 | 1.5 | 40 | + 4 | 25 |
| New 6-sections | 46 | 2500/2350/2150/1975/1600/725 | 1.5 | 40 | + 4 | 25 |
| New 6-sections | 50 | 2500/2350/2150/1975/1600/725 | 1.5 | 40 | + 4 | 25 |
| New 6-sections | 54 | 2500/2350/2150/1975/1600/725 | 1.5 | 40 | + 4 | 25 |
| New 6-sections | 58 | 2500/2350/2150/1975/1600/725 | 1.5 | 40 | +4 | 25 |
| New 6-sections | 75 | 2500/2350/2150/1975/1600/725 | 1.5 | 40 | + 4 | 25 |

Liu *et al. Chinese Journal of Mechanical Engineering*　　(2022) 35:125

Page 13 of 15



**Figure 26** Weld morphology of welded joints under different duty cycles: **a** 35%; **b** 42%; **c** 46%; **d** 50%; **e** 54%; **f** 58%; **g** 75%
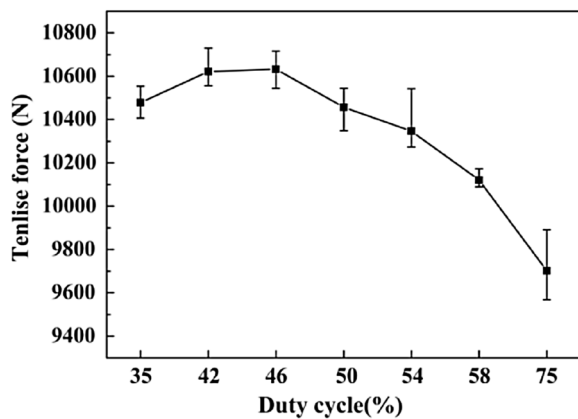


**Figure 27** Tensile shear force of welded joints under different duty cycles
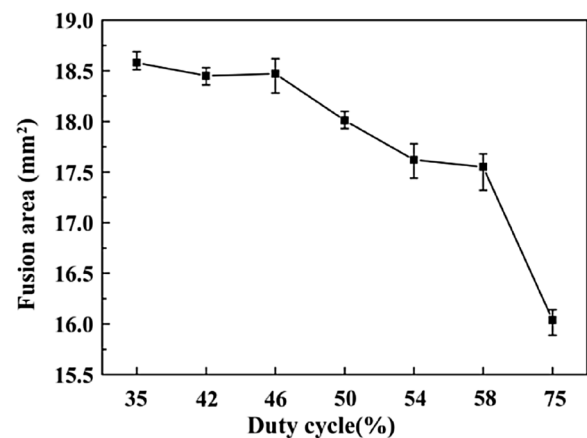


**Figure 28** Fusion area of the combined surface of the welded joint under different duty cycles

mal welding was the new 6-sections welding, which exhibited the smallest fluctuation range of depth of fusion. Its experimental results were well consistent with the simulation results.

(2) By performing the tensile test, the mechanical properties of the welded joints under different methods were obtained. With the use of the new 6-sections method, the tensile shear force was the largest. Moreover, the temperature field of the combined surface of the welded joint and the macroscopic morphology of the actual tensile fracture was analyzed. When the welding method was the new 6-section, there was no unmelted area on the combined surface of the welded joint, which also complied with the temperature field results of the numerical simulation.

(3) The variation in the duty cycle affected the pulse width of the laser. When the duty cycle ranged from 42% to 46%, the laser power density was high, the fusion area of the combined surface was large, and the formed keyhole was stable, so it hindered the formation of porosity. In this case, the resulting welded joints exhibited the highest quality.

Liu *et al. Chinese Journal of Mechanical Engineering*     (2022) 35:125

Page 14 of 15
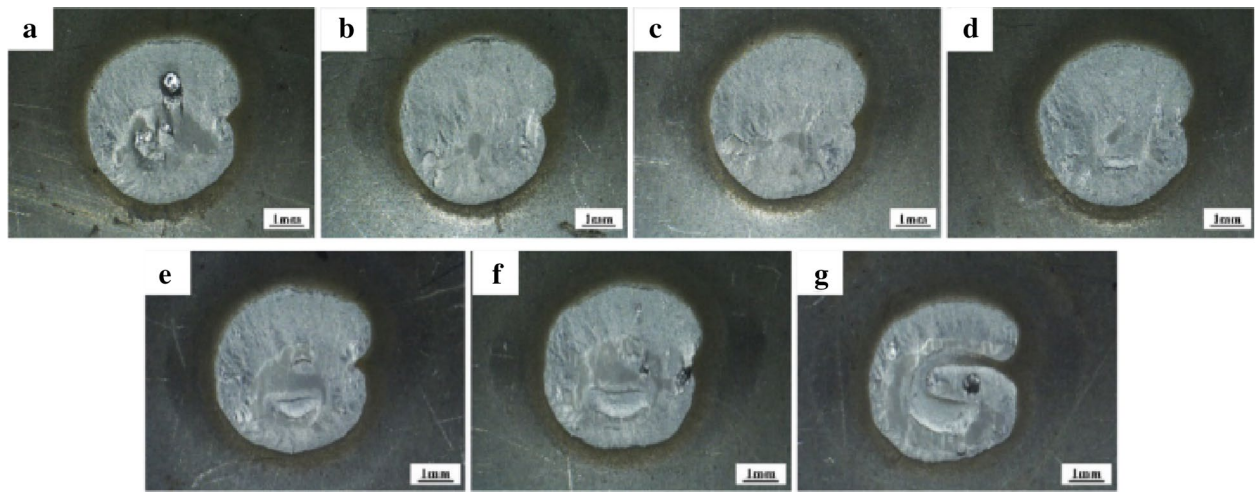


**Figure 29** Tensile fracture morphology of welded joints under different duty cycles: **a** 35%; **b** 42%; **c** 46%; **d** 50%; **e** 54%; **f** 58%; **g** 75%
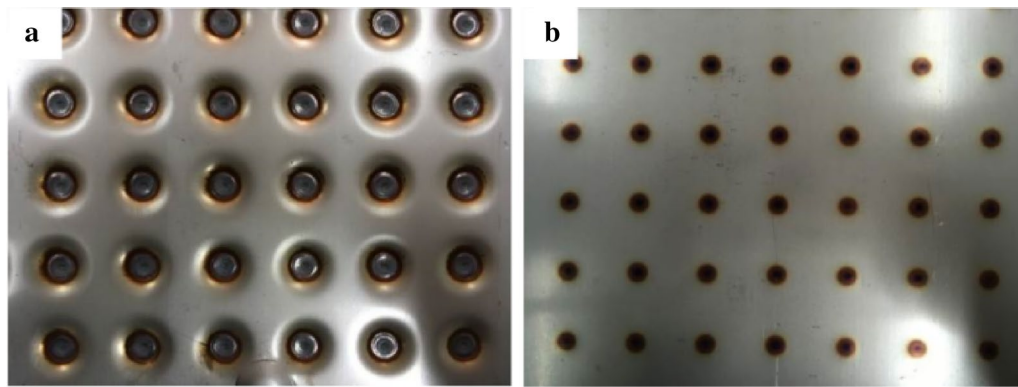


**Figure 30** Welding seam morphology of the plate-pair laser welding of the lubricating oil cooler: **a** The front side of the weld; **b** The back of the weld

**Authors' Information**
Jia Liu, born in 1983, is currently an associate professor at *Changchun University of Science and Technology, China*. He received his PhD degree from *Changchun University of Science and Technology, China*, in 2012. His research interests include laser welding, laser composite processing, and its finite element simulation technology.
Tao Jiang, born in 1992, is currently a master candidate at *Engineering Research Center of Laser Processing, Changchun University of Science and Technology, China*.
Yan Shi, born in 1972, is currently a professor at *Changchun University of Science and Technology, China*. He received his PhD degree from *Changchun University of Science and Technology, China*, in 2007.
Hongyin Zhu, born in 1994, is currently a master candidate at *Engineering Research Center of Laser Processing, Changchun University of Science and Technology, China*.

Yuchi Dai, born in 1994, is currently a PhD candidate at *Engineering Research Center of Laser Processing, Changchun University of Science and Technology, China*.

**Author Details**
[1]School of Electromechanical Engineering, Changchun University of Science and Technology, Changchun 130022, China. [2]Engineering Research Center of Laser Processing for Universities of Jilin Province, Changchun 130022, China. [3]National Base of International Science and Technology Cooperation in Optics, Changchun 130022, China.

Liu *et al. Chinese Journal of Mechanical Engineering*        (2022) 35:125

Page 15 of 15

## References

[1] M Shirzad, M A Delavar, S S M Ajarostaghi, et al. Evaluation the effects of geometrical parameters on the performance of pillow plate heat exchanger. *Chemical Engineering Research and Design*, 2019, 150: 74-83.

[2] H Kumar, N K Singh. Performance of activated TIG welding in 304 austenitic stainless steel welds. *Materials Today Proceedings*, 2017, 4(9): 9914-9918.

[3] S S Kumar, N Murugan, K K Ramachandran. Microstructure and mechanical properties of friction stir welded AISI 316L austenitic stainless steel joints. *Journal of Materials Processing Technology*, 2018, 254: 79-90.

[4] S Singh, K Hurtig, J Andersson. Investigation on effect of welding parameters on solidification cracking of austenitic stainless steel 314. *Procedia Manufacturing*, 2018, 25: 351-357.

[5] M Safari, H Mostaan, A Ghaderi. Dissimilar resistance spot welding of AISI 304 to AISI 409 stainless steels: Mechanical properties and microstructural evolutions. *Metallurgical Research and Technology*, 2018, 115(6): 610.

[6] Q Wu, J Gong, G Chen, et al. Research on laser welding of vehicle body. *Optics & Laser Technology*, 2008, 40(2): 420-426.

[7] M Gao, Y Kawahito, S Kajii. Observation and understanding in laser welding of pure titanium at subatmospheric pressure. *Optics Express*, 2017, 25(12): 13539–13548.

[8] I Miyamoto, Y Okamoto, A Hansen, et al. High speed, high strength microwelding of Si/glass using ps-laser pulses. *Optics express*, 2015, 23(3): 3427-3439.

[9] Z Y Huang, Z Luo, S S Ao, et al. Effect of Laser Welding Parameters on Weld Bowing Distortion of Thin Plates. *High Temperature Materials and Processes*, 2018, 37(4): 299-311.

[10] M Masoumi, S P H Marashi, M Pouranvari. Metallurgical and Mechanical Characterization of Laser Spot Welded Low Carbon Steel Sheets. *Steel Research International*, 2010, 81(12): 1144-1150.

[11] Y S Yang, S H Lee. A study on the joining strength of laser spot welding for automotive applications. *Journal of Materials Processing Technology*, 1999, 94(2-3): 151-156.

[12] B J Aalderink, B Pathiraj, R G K M Aarts. Seam gap bridging of laser based processes for the welding of aluminium sheets for industrial applications. *The International Journal of Advanced Manufacturing Technology*, 2010, 48(1): 143-154.

[13] J Kundu, T Ray, A Kundu, et al. Effect of the laser power on the mechanical performance of the laser spot welds in dual phase steels. *Journal of Materials Processing Technology*, 2018, 267.

[14] L F Zhao, C D Shao, Y Takashima, et al. Numerical investigation on fracture initiation properties of interface crack in dissimilar steel welded joints. *Chinese Journal of Mechanical Engineering*, 2020, 33: 27.

[15] M Dal, R Fabbro. An overview of the state of art in laser welding simulation. *Optics & Laser Technology*, 2016, 78: 2-14.

[16] K R Balasubramanian, T Suthakar, K Sankaranarayanasamy, et al. Laser Welding Simulations of Stainless Steel Joints Using Finite Element Analysis. *Advanced Materials Research*, 2012, 383-390: 6225-6230.

[17] D W Zhao, D X Ren, K M Zhao, et al. Ultrasonic welding of magnesium–titanium dissimilar metals: A study on thermo-mechanical analyses of welding process by experimentation and finite element method. *Chinese Journal of Mechanical Engineering*, 2019, 32: 97.

[18] J Yan, M Gao, X Y Zeng. Study on microstructure and mechanical properties of 304 stainless steel joints by TIG, laser and laser-TIG hybrid welding. *Optics and Lasers in Engineering*, 2010, 48(4): 512-517.

[19] M P Chakravarthy, N Ramanaiah, B S S Rao. Effect of laser welding on mechanical properties of 70/30 Cu-Ni alloy welds. *Proceedings of the Institution of Mechanical Engineers, Part B: Journal of Engineering Manufacture*, 2014, 228(9): 1153-1161.

[20] B W Liu, W T Jin, A J Lu, et al. Optimal design for dual laser beam butt welding process parameter using artificial neural networks and genetic algorithm for SUS316L austenitic stainless steel. *Optics & Laser Technology*, 2020, 125: 106027.

[21] E D Derakhshan, N Yazdian, B Craft, et al. Numerical simulation and experimental validation of residual stress and welding distortion induced by laser-based welding processes of thin structural steel plates in butt joint configuration. *Optics & Laser Technology*, 2018, 104: 170–182.

[22] S Saravanan, K Raghukandan, G S Kumaret. Comparison of numerical and experimental macrostructure in Nd: YAG laser welding of Hastelloy C-276. *Optik,* 2019, 180: 562-568.

[23] K C Ganesh, M Vasudevan, K R Balasubramanian, et al. Modeling, prediction and validation of thermal cycles, residual stress and distortion in type 316 LN stainless steel weld joint made by TIG welding process. *Procedia Engineering*, 2014, 86: 767-774.

[24] N Astafeva. Modeling of welding process and allied technologies. *Key Engineering Materials*, 2018, 69: 323-328.

[25] T Kik, J Górka. Numerical simulations of laser and hybrid S700MC T-joint welding. *Materials*, 2019, 12(3): 516.

[26] C S Wu, H G Wang, Y M Zhang. A new heat source model for keyhole plasma arc welding in FEM analysis of the temperature profile. *Welding Journal*, 2006, 85(12): 284-291.

[27] T Kik. Computational techniques in numerical simulations of arc and laser welding processes. *Materials*, 2020, 13(3): 608.

[28] W Meng, Z L Xu, Q S Ma, et al. Pulse fiber laser welding of AISI 321-AISI 405 stainless steel thick plates butt joints. *Journal of Materials Processing Technology*, 2019, 271: 214-225.

[29] Z Yang, B J Qi, B Q Cong, et al. Microstructure, tensile properties of Ti-6Al-4V by ultra high pulse frequency GTAW with low duty cycle. *Journal of Materials Processing Technology*, 2015, 216: 37-47.

[30] K Y Wu, Z Y Liang, T Yin, et al. Double pulse low-frequency modulation for high-power double-wire pulsed GMAW. *Journal of Manufacturing Science and Engineering*, 2018, 140(9): 091004.